Letter

Deconfined quantum phase transition on the kagome lattice: Distinct velocities of spinon and string excitations

Dong-Xu Liu,[1] Zijian Xiong,[1,2,3,*] Yining Xu,[3] and Xue-Feng Zhang (张学锋)[1,†]

[1]*Department of Physics, Chongqing University, Chongqing 401331, China*

[2]*Department of Applied Physics, University of Tokyo, Tokyo 113-8656, Japan*

[3]*College of Physics and Electronic Engineering, Chongqing Normal University, Chongqing 401331, China*

(Received 3 April 2023; accepted 20 March 2024; published 11 April 2024)

A deconfined quantum phase transition (DQPT) provides an extraordinary possibility of the quantum phase transition beyond the Ginzburg-Landau paradigm, which is interwoven with numerous exotic phenomena of the strongly correlated quantum many-body system, e.g., fractional excitation, emergent symmetries, and gauge field. However, various candidates of DQPT have been demonstrated to be weakly first order, and the conformal field theory has to be altered into a nonunitary one. Here we numerically found two linear dispersions with different velocities in one of the few survivors of DQPT—the extended hard-core Bose-Hubbard model on the kagome lattice. Such counterintuitive results directly lead to the negation of possible emergent Lorentz symmetry and the breakdown of conventional theory of DQPT. Furthermore, the snapshots of boson configuration hint that these two velocities may correspond to the dynamics of the fractional excitations and quantum strings, respectively. Our work will inspire researchers to revisit the theory of DQPT and benefit the field of quantum materials and quantum simulations.

DOI: 10.1103/PhysRevB.109.L140404

Introduction. The quantum phases breaking different symmetries usually undergo a discontinuous transition between them, but a deconfined quantum phase transition (DQPT) provides a prototypical counterexample, e.g., the superfluid (SF) phase can undergo a continuous transition to the valence bond solid (VBS) [1–8]. The low-energy physics of DQPT can be interpreted with two flavor spinons coupled to the U(1) gauge field [1,2]. The duality web indicates that the deconfined quantum critical point (DQCP) is either conformal invariant or flowing into the nonunitary conformal field theory (CFT) [5]. Recent research showed that most DQCP candidates belong to the nonunitary CFT [9–12]. Importantly, the proximate SU(2) DQPT was recently found in the real material $SrCu_2(BO_3)_2$ [13].

The DQPT on the kagome lattice belongs to the easy-plane type [8,14–17]. According to the field theory [5] and renormalization group (RG) analysis [17], the effective low-energy model is self-dual and supports continuous transition, so the conformal invariant is expected. Numerically, the DQPT on the kagome lattice also supports the CFT, such as the critical exponents η_{VBS} and η_{SF} being very close, and the scaling dimension of spinons is two. It is straightforward to believe that the dynamics of the system also support the conformal invariant.

In this Letter, we study the dynamics of the DQPT between the VBS and SF phases on the kagome lattice with the large-scale quantum Monte Carlo (QMC) method. As shown in Fig. 1(a), two types of linear dispersions are observed at the Γ and K points, respectively. The large deviation between their speeds is verified after careful finite-size scaling analysis, indicating the nonexistence of Lorentz symmetry at the DQCP, which conflicts with the prediction of CFT.

Model. We consider the extended hard-core Bose-Hubbard Hamiltonian [8,14–16], written as

$$H = -t\sum_{\langle i,j\rangle}(b_i^\dagger b_j + \mathrm{H.c.}) + V\sum_{\langle i,j\rangle} n_i n_j, \tag{1}$$

where $t \geqslant 0$ and $V \geqslant 0$ denote the hopping and repulsive interaction between nearest-neighbor sites, and $b_i^\dagger$ (b_i) is the creation (annihilation) operator of the hard-core boson which could be used for describing the Rydberg-dressed atom in the optical lattice [18]. After implementing the mapping $b_i^\dagger \to S_i^+$, $b_i \to S_i^-$, and $n_i \to S_i^z + 1/2$, the Hamiltonian is equivalent to the spin-half XXZ model, which is related to the quantum magnetism [19]. Because the DQPT happens at an average density equal to $1/3$, the numerical simulation is performed in the canonical ensemble [8]. Here, we choose V as the energy unit.

Minimization of the ground-state energy imposes a strong local constraint—each triangle of the kagome lattice can be occupied by only one particle (e.g., $\triangle$ or $\triangledown$, named triangle rule). Similar to the spin ice [20], the ground state is disordered with macroscopic degeneracy [21]. However, in the strong-coupling region $t/V \ll 1$, a third-order perturbative interaction $H_{\mathrm{ring}} = -\frac{12t^3}{V^2}\sum(|\hexagon\rangle\langle\hexagon| + \mathrm{H.c.})$ can exchange the configuration without breaking the triangle rule [inset of Fig. 1(a)] and lift the degeneracy so that the system enters the VBS phase. Although some spinons (e.g., $\triangle$ or Δ) can still be excited due to quantum fluctuations, the large energy gap V makes them confined.

*Corresponding author: xiongzj@cqu.edu.cn

†Corresponding author: zhangxf@cqu.edu.cn

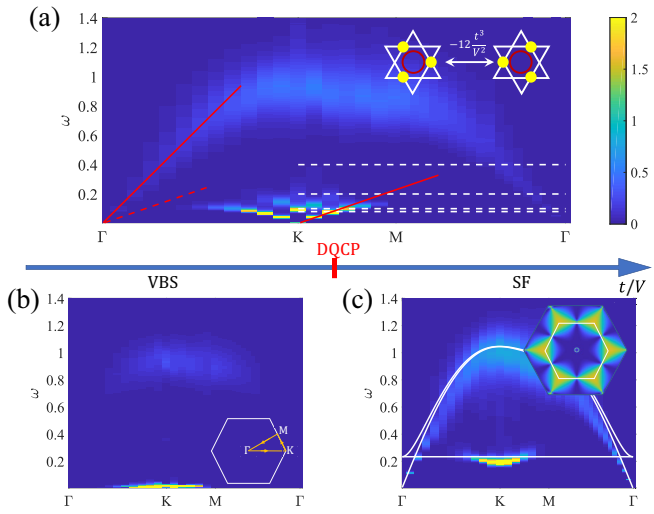

FIG. 1. The dynamic spectra of (a) DQCP at $t/V = 0.1302$, (b) VBS phase at $t/V = 0.08$, and (c) SF phase at $t/V = 0.20$ calculated with QMC simulation ($L = 36$). The inset of (a) presents ring exchange, the red solid lines show the fitting speeds at the Γ and K points (red dashed line for comparison), and the white dashed lines highlight the parameter regions in Fig. 2. The scanning path Γ-K-M-Γ is depicted in the inset of (b). The solid white lines in (c) are energy dispersion calculated by LSWT. The inset of (c) is DSF calculated by LSWT with constant energy cut close to the flat band.

In the weak-coupling region $t \gg V$, the large hopping process makes the bosons break the U(1) symmetry so that the system enters the SF phase. As shown in Fig. 1(c), with the help of linear spin wave theory (LSWT), along the selected path Γ-K-M-Γ, the lowest gapless branch at the Γ point with the linear dispersion corresponds to the Goldstone mode, and the flat-band branch results from the lattice geometry [22].

At the critical point, the interplay between the spinons and the emergent dynamical U(1) gauge field leads to the deconfined criticality. Several exotic phenomena can be found, such as the drift of the superfluid density, large anomalous critical exponent, emergent symmetries, and so on [8]. It is a common belief that this DQPT can be described by the easy-plane NCCP^1 theory [1,2].

Spectra of phases. The adopted numerical method is the stochastic cluster series expansion with parallel tempering [23], which can greatly overcome the nonergodic problem. We choose the periodic boundary condition (PBC) with the largest system size reaching $N = 36 \times 36 \times 3 = 3888$ sites. Meanwhile, in order to suppress the influence of the thermal fluctuation, the temperature is set to be $T = 1/\beta = \frac{6V}{100L}$, which is even lower than our previous work [8]. Here, we focus on the dynamical structure factor (DSF) $S^{zz}(\mathbf{k}, \omega) = \frac{1}{2\pi L^2} \sum_{ij} \int_{-\infty}^{+\infty} \mathrm{d}t\, e^{i\mathbf{k}\cdot(\mathbf{r}_i - \mathbf{r}_j) - i\omega t} \langle S_i^z(0) S_j^z(t) \rangle$, which can be extracted from the imaginary-time correlation function $S^{zz}(\mathbf{r}, \tau) = \langle S^z(\mathbf{0}, 0) S^z(\mathbf{r}, \tau) \rangle$ by implementing the stochastic analytic continuation (SAC) method [24–28]. The QMC samples are more than five million, so high-quality spectra can be obtained.

In the VBS phase, two branches can be observed in Fig. 1(b). The lower branch stays on a very low-energy scale and is nearly flat with a tiny gap (see the Supplemental Material (SM) [29]). The flat band is usually related to the lattice geometry and it reflects the localization of the particles caused by the effective ring exchange interaction [22]. Similar to the checkerboard lattice [28], it corresponds to the excitation from the triplet ground state $\frac{1}{\sqrt{2}}(|\hexagon\rangle + |\hexagon\rangle)$ to the singlet state $\frac{1}{\sqrt{2}}(|\hexagon\rangle - |\hexagon\rangle)$, so its energy scale is $\sim \frac{12t^3}{V^2}$. Meanwhile, one can see the disappearance of the flat band along the high-symmetry line Γ-M. Such fragmentation implies the existence of a "selection rule" [28,30]. On the other hand, the higher branch has a large energy gap, $\sim V$, and it is relevant to the spinon separation due to the local quantum fluctuation.

In the SF phase, the numerical spectrum in Fig. 1(c) also shows two branches. The energy scale of the flat-band branch increases a lot, while the fragmentation remains. From the LSWT calculation of DSF at the flat band [inset of Fig. 1(c)], we find no intensity along the path M-Γ, which is consistent with the numerical results. We think this fragmentation should also result from some selection rule due to the lattice symmetries [28,30]. On the other hand, the higher branch is the gapless Goldstone mode.

Spectra of DQCP. The VBS and SF phases break different symmetries, but can still undergo a continuous phase transition at DQCP between them. As shown in Fig. 1(a), at DQCP, the higher branch (named the Γ branch) is gapless at the Γ point and has a similar shape as the SF phase, but with lower intensity. Deformed from the Goldstone mode in the SF phase, the Γ branch becomes more continuous in a high-energy scale, and it indicates the emergence of the fractional charges at DQCP. Notice that here we do not choose the logarithmic scale in the ω axis, so the continuum of DSF may appear less obvious.

The lower branch (named the K branch) is largely changed and no longer flat, but the selection rule still holds. Another gapless linear mode appears at the K points, where the order parameter of the VBS phase stays. Most strikingly, it has a different speed from the Γ branch and can be clearly distinguished even with the naked eye. The dispersion of the Γ branch is faster than the K branch. This implies that the low-energy effective theory cannot be invariant under Lorentz transformations with one velocity. To obtain more details at the DQCP, we calculate the DSF over the entire first Brillouin zone. Then, the tomographic slices with fixed ω can be obtained and used for scanning the dynamics at DQCP.

The K branch has a higher intensity at low ω in comparison with the Γ branch. In Fig. 2(a), it is nearly isotropic around the K point. However, when the energy scale increases, it becomes anisotropic [Fig. 2(b)] and the U(1) symmetry is broken down to Z_3. Actually, in previous work [8,31], the histogram of the order parameter at DQCP did not exhibit the perfect emergent U(1) symmetry expected in theory. According to the NCCP^1 theory, the anisotropy may result from the threefold monopoles which are highly close to marginal [31,32]. From the dynamic spectra, we think that the possible emergent U(1) symmetry of the VBS order parameter stays at a very low-energy scale, $\sim 0.09V$, so the elimination of the anisotropy requires an extremely low temperature and large system size. At high ω, in Figs. 2(c) and 2(d), the DSF

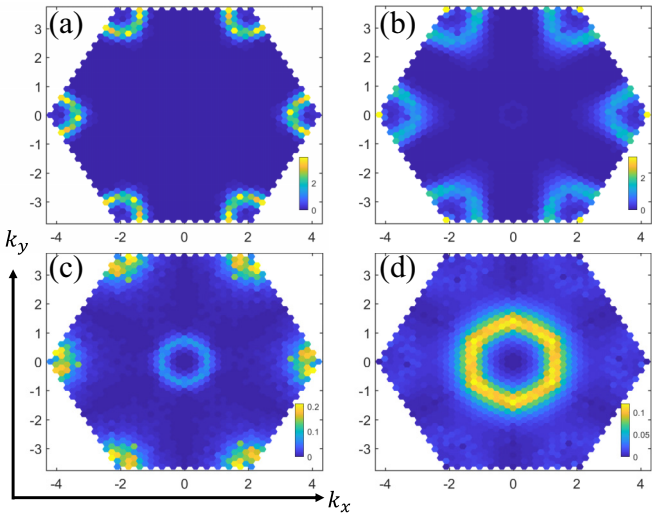

FIG. 2. The tomographic slices of DSF at DQCP calculated by QMC-SAC. The ω are fixed to (a)–(d) 0.08, 0.10, 0.20, and 0.40, respectively. The system size is $L = 36$ with inverse temperature $\beta = 600$. Because the DSF only can have a nonzero value at the reciprocal lattice site in PBC, the color in each tiny hexagon marks the value of DSF at $\mathbf{k}$ of the center of the hexagon.

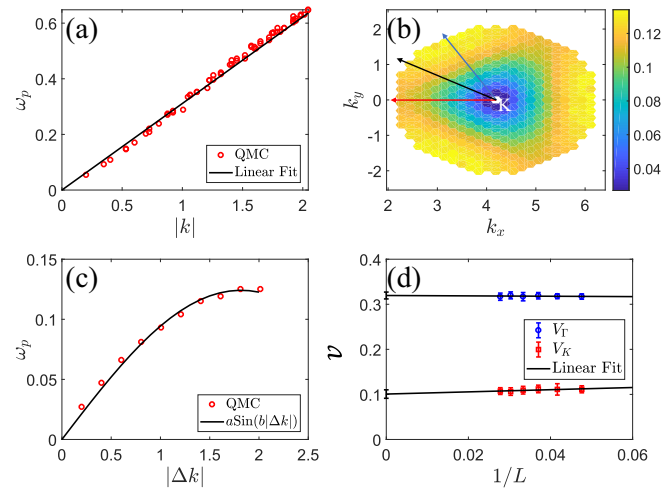

FIG. 3. The position of the peak $\omega_p(\mathbf{k})$ of (a) the Γ branch, (b) the K branch, and (c) along the angular bisector direction [black arrow in (b)]. The speed of the K branch is obtained by fitting the data along the angular bisector direction between the Γ-K direction (blue arrow) and M-K direction (red arrow). The system size is $L = 36$ with inverse temperature $\beta = 600$. (d) The finite-size scaling analysis of two speeds is performed with linear fitting the data at $L = 21, 24, 27, 30, 33, 36$ and $\beta = \frac{100L}{6V}$. The error bars on the v axis show the fitted values for the two velocities in the thermodynamic limit.

around the K point becomes messy or weaker, and no information of the K branch can be further extracted. In general, as ω increases, the Γ branch becomes clearer, while the K branch is weakened. The Γ branch is more isotropic.

Two velocities. The velocities of different modes can be extracted from the peak position of DSF $\omega_p(\mathbf{k})$ at different momentum $\mathbf{k}$. Here, to avoid introducing an additional error of unnecessary fitting, we take $\omega_p(\mathbf{k})$ at which the DSF reaches its local maximum at fixed $\mathbf{k}$. Figure 3(a) plots the relation between $\omega_p(\mathbf{k})$ and the magnitude of $\mathbf{k}$ for the Γ branch. We can find that the $\omega_p(\mathbf{k})$ depends little on the angle of $\mathbf{k}$, which firmly demonstrates the isotropy of the Γ branch. Meanwhile, the numerical data of $\omega_p(\mathbf{k})$ are in good agreement with the linear fitting result, where we obtain the constant speed of the linear dispersion at the Γ point, $V_\Gamma = 0.317(8)$ ($L = 36$).

The dispersion of the K branch is more complicated. In Fig. 3(b), the DSF around the K point presents a clear feature of anisotropy. The fastest velocity is along the M-K direction (blue arrow), and the slowest one is along the Γ-K direction (red arrow). However, both directions have only a few data points, e.g., five for $L = 36$. In contrast, there are more data points along the angular bisector direction (black arrow), e.g., 10 at $L = 36$. In order to obtain the speed of the K branch V_K with high accuracy, we fit the data along the angular bisector direction. Different from the Γ branch, the higher-energy part of the K branch exhibits a large deviation from the linearity. Actually, as shown in Fig. 3(c), we find that the sine function $\omega_p(\Delta\mathbf{k}) = a \sin b|\Delta\mathbf{k}|$ [$\Delta\mathbf{k} = \mathbf{k} - (4\pi/3, 0)$] exhibits a better fit than the linear fit. Then, the speed of the K branch can be calculated by $V_K = |ab|$. Furthermore, we want to emphasize that the anisotropy does not bring serious deviation. For example, the speeds in fast, slow, and angular bisector directions at $L = 36$ are 0.114(15), 0.103(21), and 0.107(8), respectively.

The large difference between the two speeds of the Γ branch and the K branch suggests that they originate from different physical mechanisms. First, however, we have to perform a finite-size scaling analysis to exclude possible renormalized prefactors. In Fig. 3(d), V_Γ and V_K at different system size are shown. We can find that the finite-size effects are very weak, and the numerical data match well with the linear fitting results. Finally, in the thermodynamic limit, the speed of the Γ branch is 0.319(8), and of the K branch is 0.101(9). As mentioned before, it means that there are two types of gapless quasiparticle excitations with completely different speeds, and therefore the Lorentz symmetry cannot emerge.

Phenomenological analysis. At DQCP, it is worth introducing the lattice gauge field mapping to understand the physical mechanism of topological excitations, especially the spinon (gauge charge) and the string (field line) [8,16]. As demonstrated in the left panel of Fig. 4, the hard-core boson can be mapped into the "electric field" defined at the bisector of the corner-shared triangle via the relation $E_{ll'} = n_i - 1/3$, where l is located at the center of the triangle and labels the site of the dual honeycomb lattice. The gauge charges sit on the sites of the dual lattice and can be calculated by summing over all field lines around one triangle via the "Gauss law." Meanwhile, the configurations satisfying the triangle rule are the pure gauge field, and its dynamics are mainly controlled by the ring exchange term which acts as the "magnetic field" [8,20,28]. At the DQCP, the triangle rule is broken and the spinons emerge. To better illustrate them, we set the stripe state (Fig. 4, middle panel) as the reference vacuum state (uniform electric field). Then, after subtracting the vacuum from the snapshot of the QMC configuration (Fig. 4, left panel), the spinons connected with the quantum string can be clearly observed (Fig. 4, right panel).

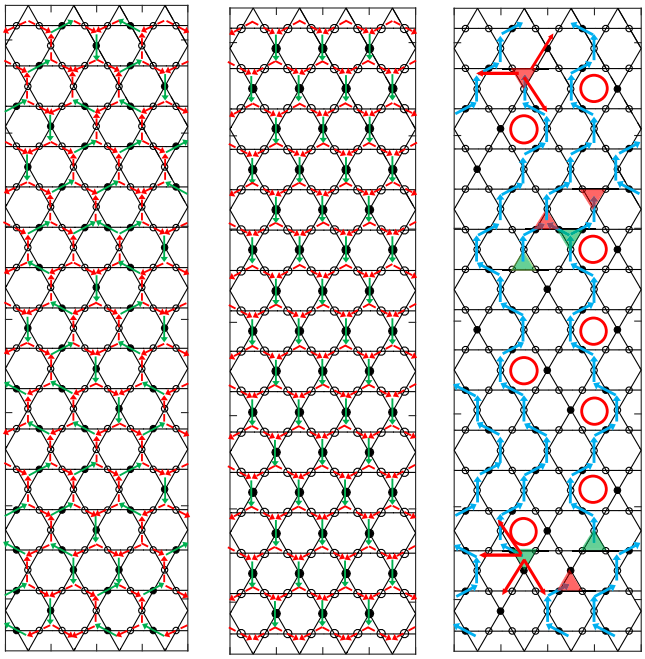

FIG. 4. Left panel: A snapshot of a typical configuration during a Monte Carlo run. Middle panel: The reference vacuum state. The red (green) arrows mark the "electric field" with a value of $-1/3$ $(2/3)$. Right panel: After subtracting the vacuum state, the open string ("electric field line") linked with the spinon ("electric charge") is shown. The red (green) triangle labels the spinon taking negative (positive) charge one. The red arrows in the right panel show the possible directions of the spinon motion. The blue arrows mark the electric field with value one. The red cycles label the hexagon where the ring exchange term can deform the string.

In the language of lattice gauge field, the nearest-neighbor hopping of bosons on the kagome lattice can be transformed into the next-nearest-neighbor hopping of the spinons in the dual honeycomb lattice (red arrows in Fig. 4, right panel). Because the honeycomb lattice is bipartite, the up-triangle and down-triangle reside in different sublattices and they correspond to different types of spinons. Thus, the low-energy physics can be approximately understood as the dynamic U(1) gauge field coupled to four types of spinons:

Type	Δ			∇
Charge	$+1$	-1	$+1$	-1
Field	p_1	h_1	p_2	h_2

As demonstrated in the right panel of Fig. 4, the possible hopping directions of the spinon are not fixed, but we can set an average hopping amplitude $t' = 7t/12$ for all the next-nearest-neighbor directions. Then, with assumption of free spinons, the energy dispersion can be obtained, $E(\mathbf{k}) = -2t'[2\cos(\frac{\sqrt{3}k_x}{2})\cos(\frac{k_y}{2}) + \cos(k_y)] \approx -t(\frac{7}{2} - \frac{7}{8}k^2)$. Similar to the Mott-SF phase transition [33], we can define the pair operator $\Psi_\alpha = (p_\alpha + h_\alpha^\dagger)/\sqrt{2}$ and $\Xi_\alpha = (p_\alpha - h_\alpha^\dagger)/\sqrt{2}$. Because the DQPT happens at exact $1/3$ filling, the densities of spinons p_α and h_α are the same. Then, after integrating out Ξ_α, the effective Lagrangian becomes "relativistic" and the velocity of the Γ branch can be estimated, $V_k \sim \sqrt{\frac{7}{8}t_c} = 0.3375$, which is close to the numerical result. Therefore, we conclude that the gapless mode of the Γ branch may be caused by the deconfinement of two types of "spinon pair" (the spectra of the off-diagonal structure factor and spinon density correlation also support that [29]).

On the other hand, the K branch is the deformation of the flat band, so it should be relevant to the effective ring exchange interaction. In previous work [16], the quantum string was well described by the spin-half XY chain at half filling. The ring exchange term is equivalent to the XY spin exchange interaction with the same strength, $t_e = -\frac{12t^3}{V^2}$. It is well known that the excitations of the spin-half XY chain are kink-antikink or the free Jordan-Wigner fermions. Then, near the Fermi point, the velocity of dispersion is $2t_e$. Because the primitive vector of the string is $\sqrt{3}/2$ times the lattice vector, the corresponding velocity should be rescaled to $4t_e/\sqrt{3} = 0.0612$, which is apparently small. Unlike Ref. [16], the quantum strings at DQCP are open strings with spinons attached to the ends, so the velocity should be strongly affected by the complex interplay between spinons and quantum strings.

Conclusion and discussion. From the dynamic spectra of DQPT on the kagome lattice, two linear dispersions are observed. The dispersion of spinons is fast and contributes to the linear dispersion of the Γ branch, and the slow linear mode at the K point may result from the internal excitation of the open quantum strings. Due to the large difference between the two speeds, the Lorentz symmetry cannot emerge at DQCP.

The DQPT on the kagome lattice is continuous, so it is not likely to be the nonunitary CFT which usually results in the weakly first order. One possibility of the CFT is that the marginal terms may make the velocities of the two modes be different. Alternatively, similar to the two velocities caused by the spin-charge separation in the one-dimensional fermionic model [34], the decoupled CFT method may also be suitable for analyzing the DQPT. Recently, there has been a different understanding of DQPT via the generalized higher-form symmetries [35], which may provide more novel understanding of these issues.

Acknowledgments. We thank Yin-Chen He, Hong-Hao Tu, Meng Cheng, Chang-Le Liu, Zheng Yan, Yan-Cheng Wang, Jin Zhang, and Zheng Zhou very much for their valuable discussions and suggestions. X.-F.Z. acknowledges funding from the National Science Foundation of China under Grants No. 12274046, No. 11874094, No.12147102, and No.12347101, the Chongqing Natural Science Foundation under Grant No. CSTB2022NSCQ-JQX0018, the Fundamental Research Funds for the Central Universities Grant No. 2021CDJZYJH-003, and the Xiaomi Foundation/Xiaomi Young Talents Program. Z.X. acknowledges funding from the International Postdoctoral Exchange Fellowship Program 2022 by the Office of China Postdoctoral Council (Grant No. PC2022072) and the National Natural Science Foundation of China (Grant No. 12147172). Y.X. is supported by the Natural Science Foundation of Chongqing (Grant No. cstc2021jcyj-msxmX0428) and by the Science and Technology Research Program of Chongqing Municipal Education Commission (Grant No. KJQN202100514).

[1] T. Senthil, A. Vishwanath, L. Balents, S. Sachdev, and M. P. A. Fisher, Deconfined quantum critical points, Science **303**, 1490 (2004).

[2] T. Senthil, L. Balents, S. Sachdev, A. Vishwanath, and M. P. A. Fisher, Quantum criticality beyond the Landau-Ginzburg-Wilson paradigm, Phys. Rev. B **70**, 144407 (2004).

[3] A. W. Sandvik, Evidence for deconfined quantum criticality in a two-dimensional Heisenberg model with four-spin interactions, Phys. Rev. Lett. **98**, 227202 (2007).

[4] A. Nahum, J. T. Chalker, P. Serna, M. Ortuño, and A. M. Somoza, Deconfined quantum criticality, scaling violations, and classical loop models, Phys. Rev. X **5**, 041048 (2015).

[5] C. Wang, A. Nahum, M. A. Metlitski, C. Xu, and T. Senthil, Deconfined quantum critical points: Symmetries and dualities, Phys. Rev. X **7**, 031051 (2017).

[6] Y. Q. Qin, Y.-Y. He, Y.-Z. You, Z.-Y. Lu, A. Sen, A. W. Sandvik, C. Xu, and Z. Y. Meng, Duality between the deconfined quantum-critical point and the bosonic topological transition, Phys. Rev. X **7**, 031052 (2017).

[7] Y. Liu, Z. Wang, T. Sato, M. Hohenadler, C. Wang, W. Guo, and F. F. Assaad, Superconductivity from the condensation of topological defects in a quantum spin-Hall insulator, Nat. Commun. **10**, 2658 (2019).

[8] X.-F. Zhang, Y.-C. He, S. Eggert, R. Moessner, and F. Pollmann, Continuous easy-plane deconfined phase transition on the kagome lattice, Phys. Rev. Lett. **120**, 115702 (2018).

[9] Y.-C. Wang, N. Ma, M. Cheng, and Z. Y. Meng, Scaling of the disorder operator at deconfined quantum criticality, SciPost Phys. **13**, 123 (2022).

[10] Z. H. Liu, W. Jiang, B.-B. Chen, J. Rong, M. Cheng, K. Sun, Z. Y. Meng, and F. F. Assaad, Fermion disorder operator at Gross-Neveu and deconfined quantum criticalities, Phys. Rev. Lett. **130**, 266501 (2023).

[11] R. Ma and C. Wang, Theory of deconfined pseudocriticality, Phys. Rev. B **102**, 020407(R) (2020).

[12] Y. Da Liao, G. Pan, W. Jiang, Y. Qi, and Z. Y. Meng, The teaching from entanglement: 2D SU(2) antiferromagnet to valence bond solid deconfined quantum critical points are not conformal, arXiv:2302.11742.

[13] Y. Cui, L. Liu, H. Lin, K.-H. Wu, W. Hong, X. Liu, C. Li, Z. Hu, N. Xi, S. Li, R. Yu, A. W. Sandvik, and W. Yu, Proximate deconfined quantum critical point in $SrCu_2(BO_3)_2$, Science **380**, 1179 (2023).

[14] K. Damle and T. Senthil, Spin nematics and magnetization plateau transition in anisotropic kagome magnets, Phys. Rev. Lett. **97**, 067202 (2006).

[15] S. V. Isakov, S. Wessel, R. G. Melko, K. Sengupta, and Y. B. Kim, Hard-core bosons on the kagome lattice: Valence-bond solids and their quantum melting, Phys. Rev. Lett. **97**, 147202 (2006).

[16] X.-F. Zhang and S. Eggert, Chiral edge states and fractional charge separation in a system of interacting bosons on a kagome lattice, Phys. Rev. Lett. **111**, 147201 (2013).

[17] V. Shyta, J. van den Brink, and F. S. Nogueira, Frozen deconfined quantum criticality, Phys. Rev. Lett. **129**, 227203 (2022).

[18] S. Hollerith, K. Srakaew, D. Wei, A. Rubio-Abadal, D. Adler, P. Weckesser, A. Kruckenhauser, V. Walther, R. van Bijnen, J. Rui, C. Gross, I. Bloch, and J. Zeiher, Realizing distance-selective interactions in a Rydberg-dressed atom array, Phys. Rev. Lett. **128**, 113602 (2022).

[19] T.-H. Han, J. S. Helton, S. Chu, D. G. Nocera, J. A. Rodriguez-Rivera, C. Broholm, and Y. S. Lee, Fractionalized excitations in the spin-liquid state of a kagome-lattice antiferromagnet, Nature (London) **492**, 406 (2012).

[20] L. Savary and L. Balents, Coulombic quantum liquids in spin-1/2 pyrochlores, Phys. Rev. Lett. **108**, 037202 (2012).

[21] L. Pauling, The structure and entropy of ice and of other crystals with some randomness of atomic arrangement, J. Am. Chem. Soc. **57**, 2680 (1935).

[22] P. Pudleiner and A. Mielke, Interacting bosons in two-dimensional flat band systems, Eur. Phys. J. B **88**, 207 (2015).

[23] P. Sengupta, A. W. Sandvik, and D. K. Campbell, Bond-order-wave phase and quantum phase transitions in the one-dimensional extended Hubbard model, Phys. Rev. B **65**, 155113 (2002).

[24] H. Shao and A. W. Sandvik, Progress on stochastic analytic continuation of quantum Monte Carlo data, Phys. Rep. **1003**, 1 (2023).

[25] H. Shao, Y. Q. Qin, S. Capponi, S. Chesi, Z. Y. Meng, and A. W. Sandvik, Nearly deconfined spinon excitations in the square-lattice spin-1/2 Heisenberg antiferromagnet, Phys. Rev. X **7**, 041072 (2017).

[26] N. Ma, G.-Y. Sun, Y.-Z. You, C. Xu, A. Vishwanath, A. W. Sandvik, and Z. Y. Meng, Dynamical signature of fractionalization at a deconfined quantum critical point, Phys. Rev. B **98**, 174421 (2018).

[27] Z. Zhou, C. Liu, Z. Yan, Y. Chen, and X.-F. Zhang, Quantum dynamics of topological strings in a frustrated Ising antiferromagnet, npj Quantum Mater. **7**, 60 (2022).

[28] Z. Xiong, Y. Xu, and X.-F. Zhang, Dynamics in the planar pyrochlore lattice: Bow-tie flat band and mixed 't Hooft anomaly, arXiv:2111.11445.

[29] See Supplemental Material at http://link.aps.org/supplemental/10.1103/PhysRevB.109.L140404 for a further discussion of the finite-size scaling of the energy gap and other dynamical spectra, which also includes Refs. [8,27,36,37].

[30] Z. Xiong, 1-form symmetry and the selection rule of the plaquette valence bond solid phase on the kagome lattice, Phys. Rev. B **108**, 195107 (2023).

[31] S. Pujari, K. Damle, and F. Alet, Néel-state to valence-bond-solid transition on the honeycomb lattice: Evidence for deconfined criticality, Phys. Rev. Lett. **111**, 087203 (2013).

[32] M. S. Block, R. G. Melko, and R. K. Kaul, Fate of $\mathbb{CP}^{N-1}$ fixed points with q monopoles, Phys. Rev. Lett. **111**, 137202 (2013).

[33] L. Balents, L. Bartosch, A. Burkov, S. Sachdev, and K. Sengupta, Competing orders and non-Landau-Ginzburg-Wilson criticality in (Bose) Mott transitions, Prog. Theor. Phys. Suppl. **160**, 314 (2005).

[34] Y. Jompol, C. J. B. Ford, J. P. Griffiths, I. Farrer, G. A. C. Jones, D. Anderson, D. A. Ritchie, T. W. Silk, and A. J. Schofield, Probing spin-charge separation in a Tomonaga-Luttinger liquid, Science **325**, 597 (2009).

[35] J. McGreevy, Generalized symmetries in condensed matter, Ann. Rev. **14**, 57 (2023).

[36] J. Becker and S. Wessel, Diagnosing fractionalization from the spin dynamics of Z_2 spin liquids on the kagome lattice by quantum Monte Carlo simulations, Phys. Rev. Lett. **121**, 077202 (2018).

[37] C.-J. Huang, Y. Deng, Y. Wan, and Z. Y. Meng, Dynamics of topological excitations in a model quantum spin ice, Phys. Rev. Lett. **120**, 167202 (2018).